Supporting Information

Case study evaluation of size-resolved molecular composition and phase state of carbonaceous particles in wildfire influenced smoke from the Pacific Northwest

Gregory W. Vandergrift;[1] Nurun Nahar Lata;[1] Susan Mathai;[1,2] Amna Ijaz;[1,2,†] Zezhen Cheng;[1] Manish Shrivastava;[3] Jie Zhang;[3] Abu Sayeed Md Shawon;[1,2,§] Gourihar Kulkarni;[3] Lynn R. Mazzoleni;[2] William Kew;[1] Swarup China[1]*

[1] Environmental Molecular Sciences Laboratory, Pacific Northwest National Laboratory (PNNL), Richland, Washington 99352, USA

[2] Atmospheric Sciences Program, Michigan Technological University, Houghton, Michigan, 49921, USA

[3] Atmospheric Sciences and Global Change Division, Pacific Northwest National Laboratory (PNNL), Richland, Washington 99352, USA

Current Addresses

† Laboratoire de Chimie Environnement, Université d'Aix-Marseille, Marseille, 13007, France.

§ Earth and Environmental Sciences Division, Los Alamos National Laboratory, Los Alamos, NM 87545, USA

* Address correspondence to Swarup.China@pnnl.gov

Sample Collection

Particle samples were collected on August 2 and the following nighttime of August 3, 2021 at the Pacific Northwest National Lab (Richland, WA). Particles were collected onto Teflon filters (Whatman) and TEM grids (Tedpella) using using 10-stage Micro-Orifice Uniform Deposition Impactors (MOUDI; model 110-R, MSP, Inc.). Samples were collected on stage 7 (0.32-0.56 µm), stage 8 (0.18-0.32 µm), and stage 9 (0.10-0.18 µm). Teflon filters were used for high resolution mass spectrometry analysis while TEM grids were used for multi-modal micro-spectroscopy analysis.

Table S1: Summary of date, time, and meteorological conditions for periods of day and nighttime sampling. Reported uncertainties are representative of standard deviations.

Sample	Date	Sampling Time (PST)	Temperature (°C)	Relative Humidity (%)
Day	August 2, 2021	3:53 PM – 4:50 PM	37.7 ± 0.3	23 ± 3
Night	August 3, 2021	8:35 PM – 1:00 AM	30 ± 3	34 ± 7

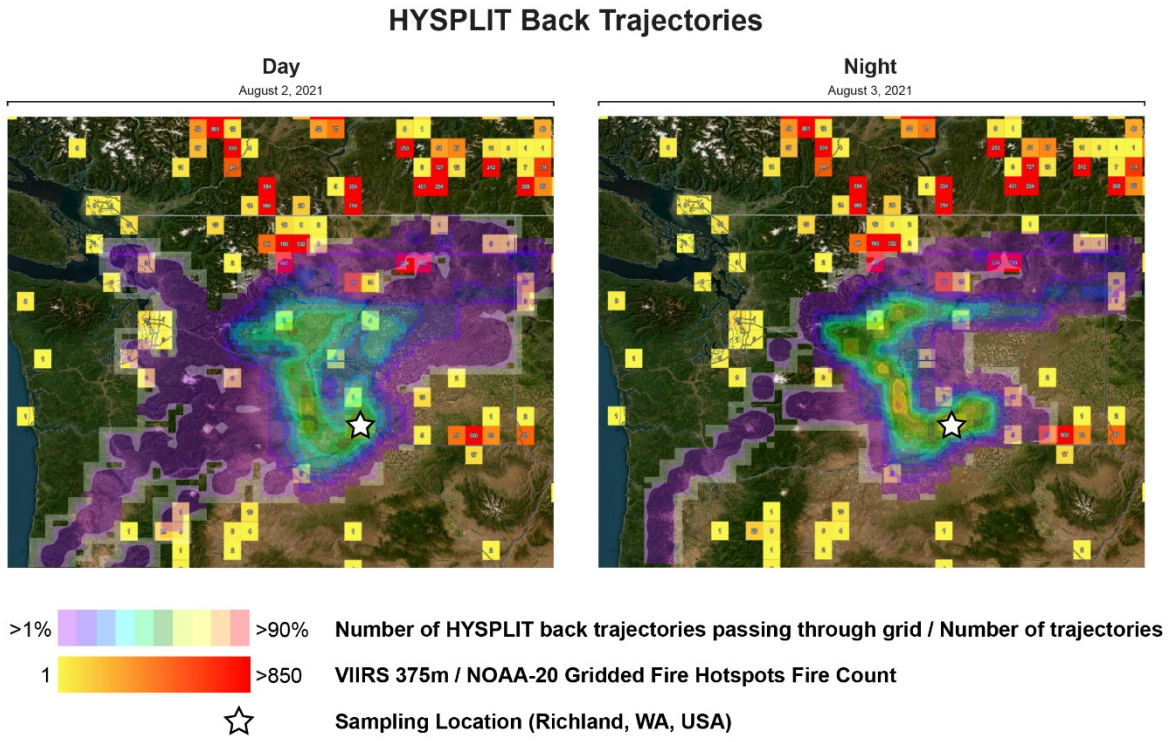

Figure S1. 72-hour HYSPLIT back trajectory frequencies (25 m height, 3 hour trajectory starting interval, 24 total trajecties per sample) for atmospheric aerosol collected in Richland, WA. VIIRS (Visible Infrared Imaging Radiometer Suite) data from NASA is overlaid to show the locations of active wildfires.

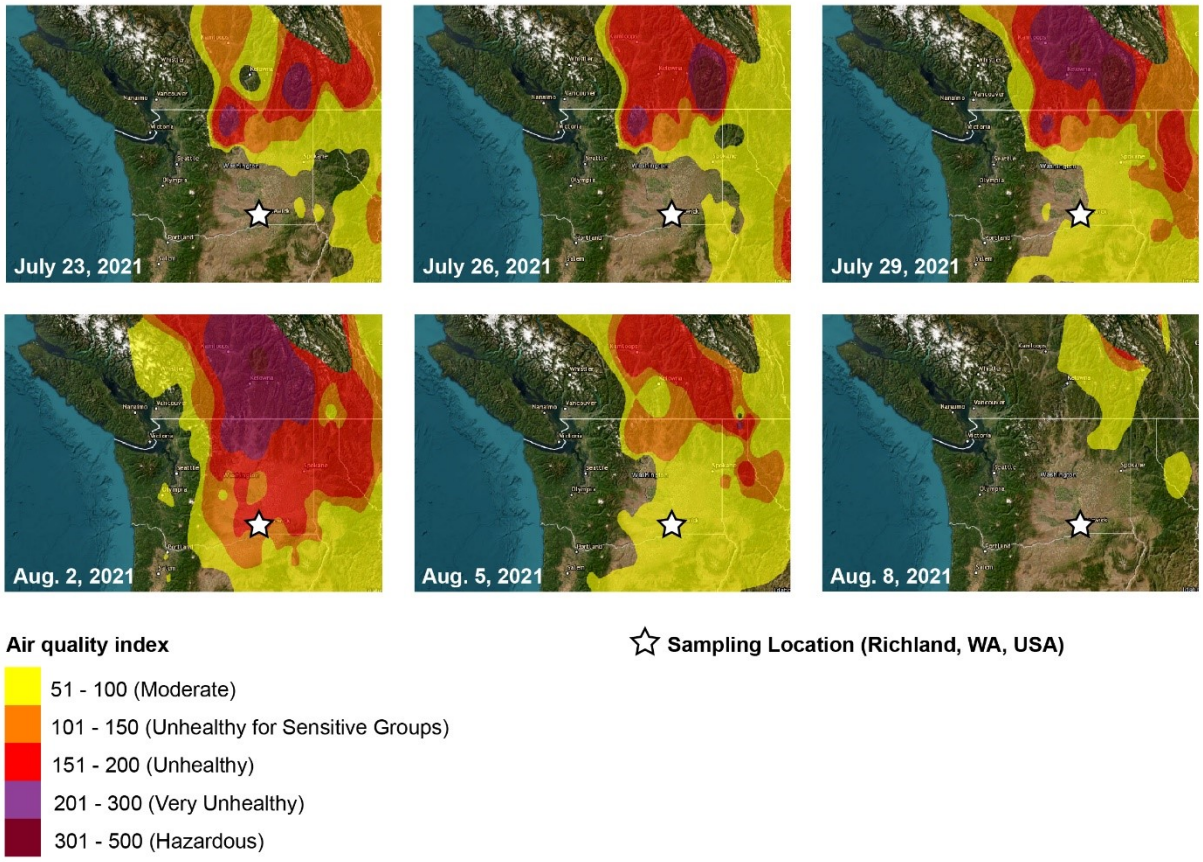

Figure S2. Air quality index (AQI) contours for July 23 through August 8, 2021. Data was accessed from the 'AirNow' resource.[1]

Auxiliary Aerosol Measurements

A TSI Scanning Mobility Particle Sizer (SMPS) was used to measure the particle electrical-mobility size distribution (from 14 to 710 nm) from August 2 – 4, 2021. The SMPS includes an Electrostatic Classifier (Model 3080, TSI), a neutralizer (TSI), a long Differential Mobility Analyzer (DMA, Model 3081, TSI), an impactor nozzle (50 % cutoff size at 1 µm), and a Condensation Particle Counter (CPC, Model 3775, TSI). Figure S3 shows the normalized particle electrical-mobility size distribution and the total particle concentration measured by SMPS at the sampling site. Shaded areas represent two sample collection periods (day and nighttime) used for this study. The average total particle concentrations for day and nighttime sampling periods were comparable (~2200 particles cm^{-3} and ~1700 particles cm^{-3}, respectively). Figure S4 shows the normalized columnar volume particle size distribution and total columnar particle volume concentration from August 2 – 4, 2021, which was provided by AErosol RObotic NETwork (AERONET) Version 3.0 algorithm products and quality level 1.5 at the Pacific Northwest National Laboratory (PNNL) site (46.341° N, 119.279° W).

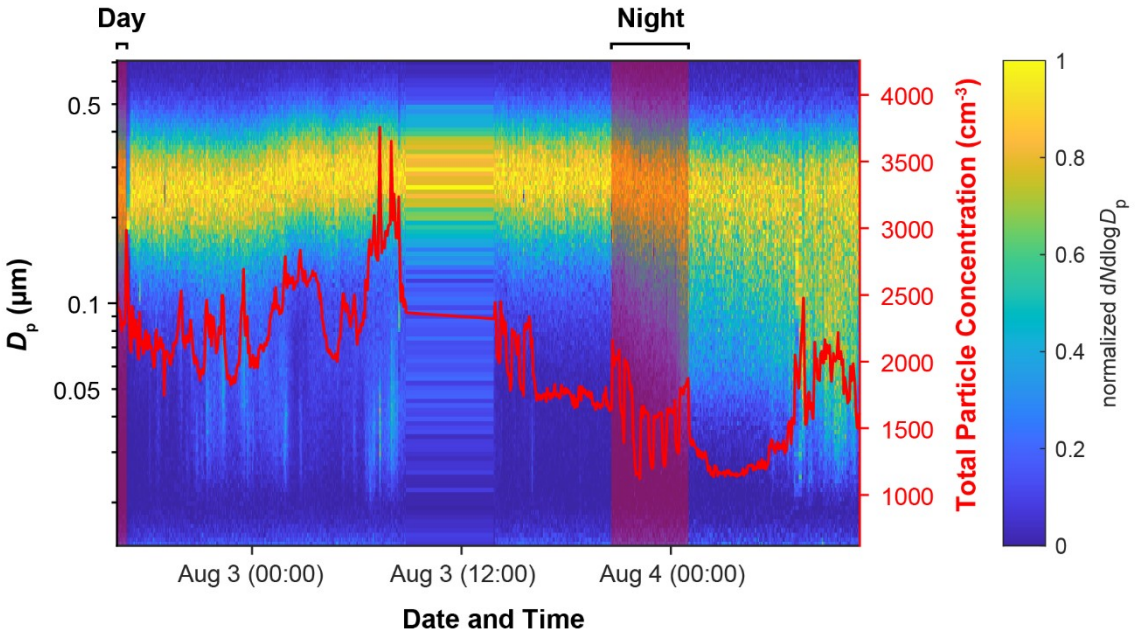

Figure S3. Scanning Mobility Particle Sizer (SMPS) data for the particle electrical-mobility size distribution (from 14 to 710 nm) and total particle concentration as measured from August 2 – 4, 2021. Shaded red regions correspond to sampling periods for day and nighttime as used in this study.

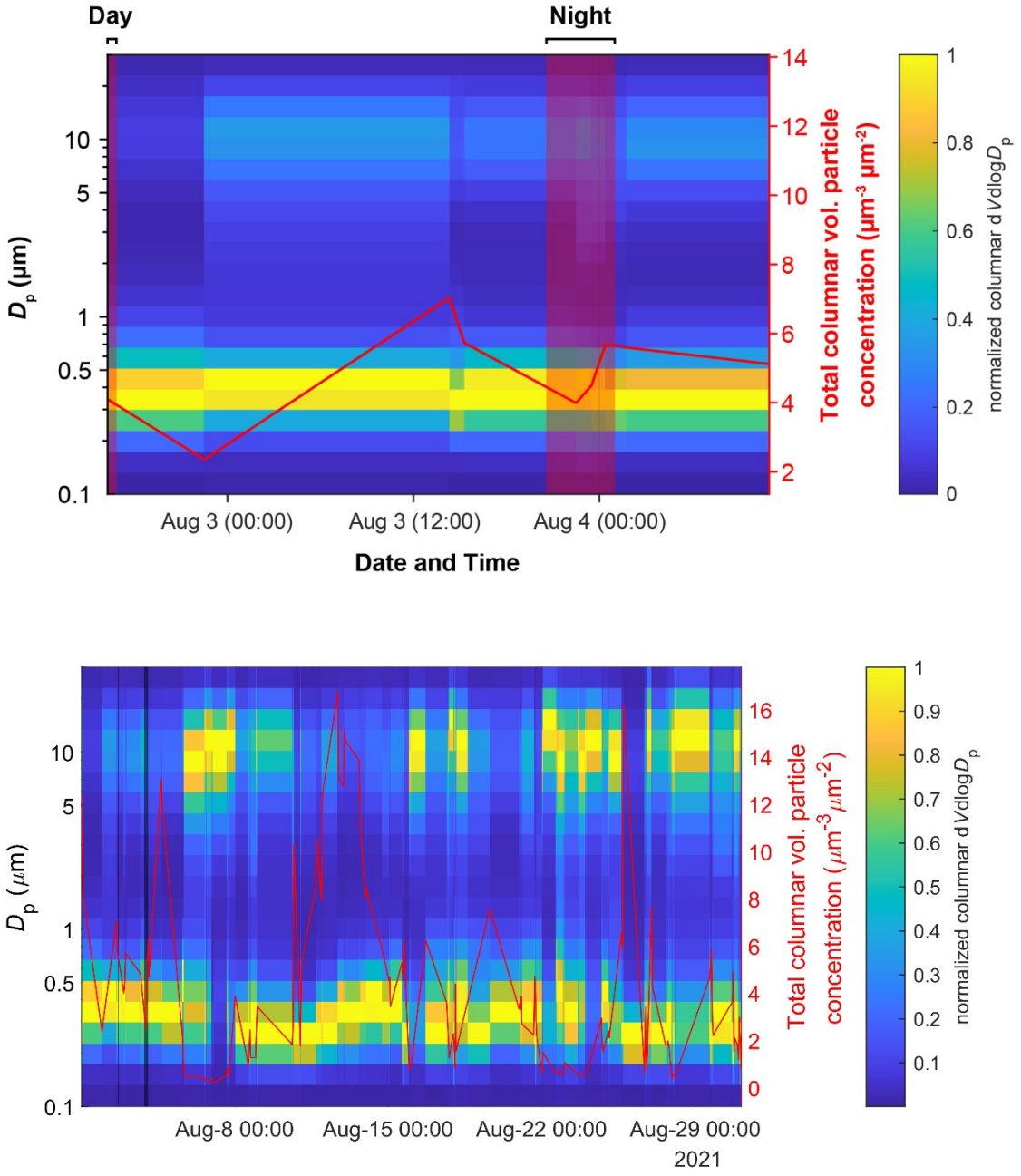

Figure S4: Normalized columnar volume particle size distribution and total columnar particle volume concentration from August 2 – 4, 2021 (top) as well as for the entirety of August 2021 (bottom). Data was provided via the AErosol RObotic NETwork (AERONET) Version 3.0 algorithm products and quality level 1.5 at the Pacific Northwest National Laboratory (PNNL) site (46.341° N, 119.279° W). Shaded regions (red for top figure, black for bottom) correspond to sampling periods for day and nighttime as used in this study.

Additional details for microspectroscopic analysis of individual particles

Carbon K-edge X-ray absorption spectra were obtained by scanning particles between 278 and 320 eV at 111 different carbon K-edge energies called “stacks” whereas “maps” were collected at less number of energies (11 energies) to get a better statistical sampling of the particle population with faster image collection (25 nm spatial resolution).

Particle phase states as determined by measured aspect ratios (width to height) from ESEM data has been described elsewhere by Cheng *et al*.[2] Briefly, the suggested glass transition to ambient temperature (T_g/T_{amb}) thresholds proposed by Shiraiwa *et al.*[3] and Schmedding *et al.*[4] (solid-like for $T_g/T_{amb} > 1$, semi-solid-like for $1 \leq T_g/T_{amb} < 0.8$, liquid-like for $T_g/T_{amb} \leq 0.8$) were used to predict phase state. In Cheng *et al.*, T_g was calculated as a function of relative humidity (RH), showing that T_g/T_{amb} ratios of 0.8 and 1 corresponded to RH of 89% and 97%, respectively. At these RHs, the particle aspect ratios were measured to be 1.30 and 1.85, respectively. Therefore, Cheng *et al.* proposed that particles are in a solid-like state for aspect ratios less than 1.30, in a semi-solid state for aspect ratios between 1.30 and 1.85, and in a liquid-like state for aspect ratios greater than 1.85. These constraints for estimating particle phase state are applied here.

Particle phase states as determined from STXM – NEXAFS datasets have similarly used particle aspect ratio to infer phase state, where particle height (analogous to path length within the context of the Beer-Lambert law) is inferred from total carbon absorption (TCA) meausrements. This strategy has been employed in several previous studies.[5–7]

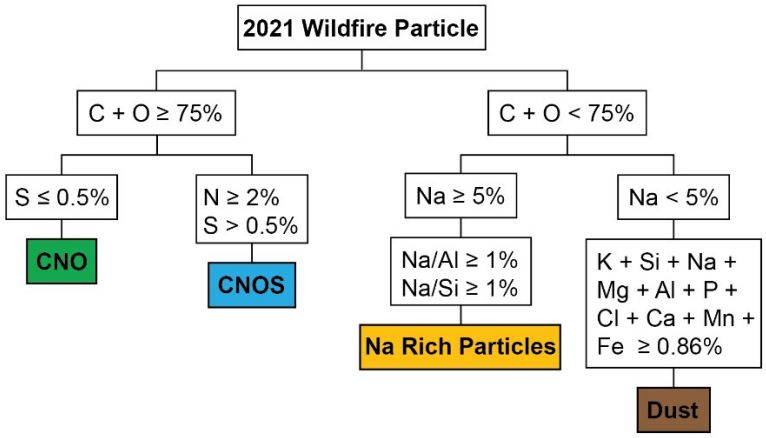

Figure S5: Particle classification system for particles measured by computer-controlled scanning electron microscopy with energy-dispersive X-ray spectroscopy (CCSEM – EDX) via k-means clustering (elbow method).[8]

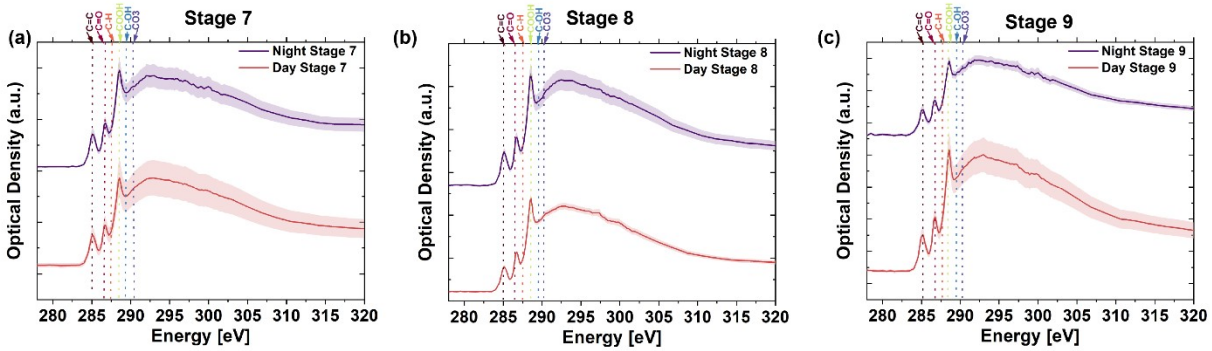

Figure S6: Carbon – potassium edge scanning transmission X-ray microscopy with near-edge X-ray absorption fine structure spectroscopy (STXM – NEXAFS) spectra obtained for stages 7 – 9 and for periods of day and nighttime. Shaded areas represent measurement uncertainties.

Table S2: Spectral deconvolution parameters for scanning transmission X-ray microscopy with near-edge X-ray absorption fine structure spectroscopy (STXM – NEXAFS).

Energy (eV)	Transition	Functional Group	Width (eV)	References
285.1	1s→π*	'C*=C'	1.19 ± 0.30	[9,10]
286.7	K1s→π* or K1s→π*	C=O' or C*OH	0.96 ± 0.222	[10,11]
287.7	K1s→C*H	'C*H'	1.0 ± 0.11	[6,10,12]
288.3	K1s→π*	'NH(C*=O)'	0.36 ± 0.019	[6,10,12]
288.5	K1s→π*	'COOH'	1.0 ± 0.18	[10–13]
289.5	K1s→π*	'C-OH'	1.3 ± 0.063	[10–14]
290	Edge Step	Total Carbon	2 .0 ± 0.20	[10–14]
290.4	K1s→ π*	C*O3	0.72 ± 0.08	[10–14]
297.1	$L_2 2p_{1/2}$	K*	1.20 ± 0.40	[10–14]
299.7	$L_3 2p_{3/2}$	K*	0.82 ± 0.31	[10–14]
300.4	1s→σ*	C*=C, C*=O	4.08 ± 1.25	[10–14]

Additional details for nano-DESI 21T FTICR MS analyses

The nano-DESI assembly was constructed using identical capillary geometries for both primary and secondary capillaries (150 µm O.D., 50 µm I.D.) meeting at a ~80° angle, through which a 7/3 acetonitrile/water *v/v* solvent mixture was flowed at 500 nL/min. -3.5 kV was applied via the solvent syringe needle. The nano-DESI assembly was then brought sufficiently close to an aerosol filter substrate, allowing a liquid micro-junction to be established. The liquid micro-junction was maintained while scanning along XY plane at 35 µm/s, allowing for constant desorption/ionization of aerosol material. The MS inlet was maintained at 250°C, and a maximum ion injection time of 250 ms was allowed to reach an automatic gain control (AGC target) of 5×10^5. For data collection, 150 MS1 scans were collected per sample, and averaged within Xcalibur (Thermo Scientific) before export as a .csv peak list (5 decimals per MS feature). The resultant .csv was noise-thresholded (noise defined as the standard deviation for *m/z* 625 – 700 peak intensities) according to a signal-to-noise ratio of 6. The resultant peak list was subjected to molecular formulae assignment. After verifying minimal to no contribution from S and P heteroatoms, additional restrictions for formula assignment were used: $0.3 \leq H/C \leq 3$; $O/C \leq 2.5$;

−20 ≤ DBE-O ≤ 25 (DBE-O: double bond equivalents minus oxygen count). No blank subtraction was conducted

Equations used for various parametrizations of the mass spectrometry data are described below along with appropriate references:

Eq. S1) $$DBE = C + 1 - \frac{1}{2}H + \frac{1}{2}N$$

Eq. S2)[15] $$OS_C \approx 2\frac{O}{C} - \frac{H}{C} - 5\frac{N}{C} - 6\frac{S}{C}$$

Eq. S3)[16] $$\log_{10} C_0 = \left(n_C^0 - n_C\right)b_C - n_O b_O - n_H b_H - 2\frac{n_C n_O}{n_C + n_O}b_{CO} - n_N b_N - n_S b_S$$

Group	n_C^0	b_C	b_H	b_O	b_{CO}	b_N	b_S
CHO	15.77	0.6238	-0.1387	1.735	-0.8592	0	0
CHNO	21.12	0.4139	-0.0376	0.8092	-0.1174	1.1010	0

Eq. S4)[17,18] $$AI_{mod} = \frac{1 + C - \frac{1}{2}O - S - \frac{1}{2}H - \frac{1}{2}N}{C - \frac{1}{2}O - S - N}$$

Aliphatic: $AI_{mod} \leq 0$

Low O Unsaturated: $0 < AI_{mod} \leq 0.5$ and $O/C < 0.5$

High O Unsaturated: $0 < AI_{mod} \leq 0.5$ and $O/C \geq 0.5$

Aromatic: $0.5 < AI_{mod} < 0.67$

$AI_{mod} \geq 0.67$ and $C < 8$

Condensed Aromatic: $AI_{mod} \geq 0.67$ and $C \geq 8$

Complete description of all variables intrinsic to each equation are available in the primary references cited within the main manuscript.

Additional details for evaporation kinetics modelling

The time-dependent evaporation of multicomponent SOA particles is modeled by solving mass transfer equations assuming that particles are suspended in the organic-free gas, where the organic vapors are removed by activated charcoal during the entire simulations. We used a 14-bin volatility basis set with saturation mass concentration (C^*) ranging from 10^{-9} to 10^4 μg m^{-3} to represent the gas-particle partitioning of biomass burning OA. Each simulation was conducted at a constant room temperature of 298 K such that the enthalpy of vaporization does not affect calculations. Estimations of the initial mass fraction of each volatility bin (based upon parametrized volatilies weighted to mass spectrometry signal intensities) are presented Table S3. Initial particle diameters are also shown. The molecular weight of

lumped species was assumed to be 200 g mol^{-1}; the air density is 1200 kg m^{-3}; the diffusion coefficient is 5.7×10^{-6} m^2 s^{-1}; and surface tension is 0.07 N m^{-1} based on Upshur *et al.*[19] The initial (t = 0 hrs) and final (t = 23 hrs) predicted mass fractions for each volatility bin are shown in Figure S4. More detailed model descriptions and related calculation can be found in the Supplementary Information of Vaden *et al.*[20]

Table S3: The initial particle diameter (*Dp*) and weighted mass spectrometry intensities for each volatility bin for stages 7, 8, and 9 of wildfire-influenced aerosol collected during periods of both day (August 2, 2021) and nighttime (August 3, 2021).

	Daytime (August 2, 2021)			**Nighttime (August 3, 2021)**		
	Stage 7	Stage 8	Stage 9	Stage 7	Stage 8	Stage 9
Initial *Dp* (µm)	0.44	0.25	0.14	0.44	0.25	0.14
*C** (µg m^{-3})	Parametrized volatilities weighted to MS signal intensities					
10^{-9}	0.151	0.149	0.113	0.139	0.125	0.087
10^{-8}	0.061	0.058	0.054	0.055	0.053	0.048
10^{-7}	0.067	0.062	0.060	0.060	0.060	0.054
10^{-6}	0.070	0.069	0.073	0.065	0.068	0.060
10^{-5}	0.083	0.080	0.081	0.076	0.080	0.072
10^{-4}	0.096	0.093	0.095	0.092	0.098	0.093
10^{-3}	0.092	0.092	0.099	0.096	0.098	0.102
10^{-2}	0.085	0.089	0.093	0.092	0.094	0.098
10^{-1}	0.090	0.091	0.096	0.094	0.095	0.103
10^{0}	0.091	0.092	0.101	0.097	0.098	0.116
10^{1}	0.071	0.079	0.084	0.081	0.082	0.103
10^{2}	0.027	0.029	0.033	0.033	0.031	0.041
10^{3}	0.015	0.017	0.017	0.018	0.017	0.023
10^{4}	0.001	0.001	0.001	0.001	0.001	0.001

Table S4: Weighted volatilities and standard deviations (according to signal intensities from mass spectrometry) for stages 7, 8, and 9 of wildfire aerosol collected during periods of both day (August 2, 2021) and nighttime (August 3, 2021).

	Weighted $Log_{10}(C_0$ / µg $m^{-3})$	
	Day August 2, 2021	Night August 3, 2021
Stage 7	-3.6	-3.3
Stage 8	-3.5	-3.2
Stage 9	-3.1	-2.9

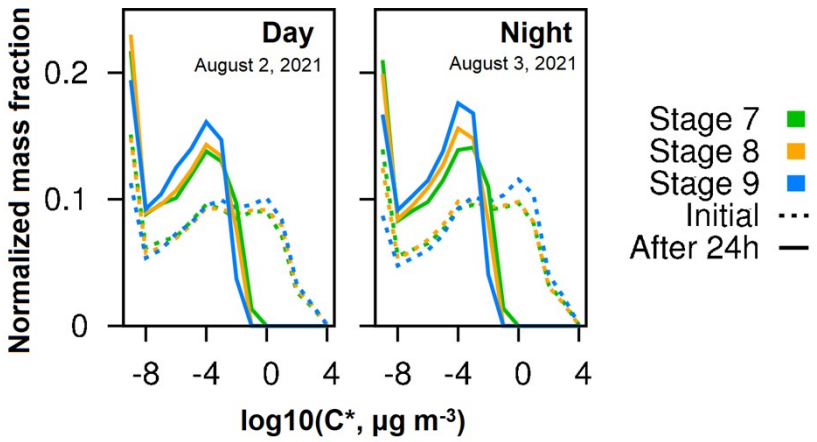

Figure S7: Simulated volatility distributions of biomass burning OA at the end of 24 hours of evaporation in an organic gas-free environment at room temperature (solid lines with different colors for the stages 7, 8 and 9). Dashed lines show the initial volatility distributions for each stage.

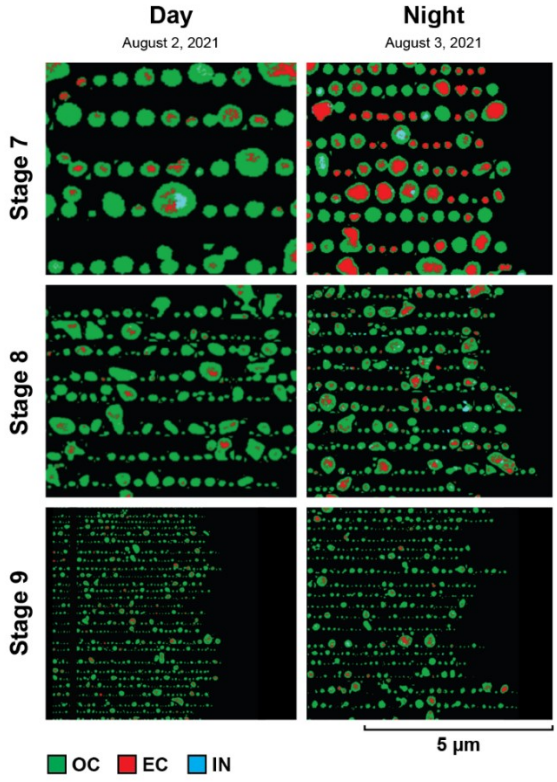

Figure S8: Distribution of organic and inorganic components in representative wildfire particles from stages 7 through 9 for periods of both day and nighttime as measured by scanning transmission X-ray microscopy with near-edge X-ray absorption fine structure spectroscopy (STXM – NEXAFAS). Note that the diagrammatic representations of particle size are to scale for aerodynamic particles, and not those that are impacted onto the surface used for STXM – NEXAFS analysis.

Table S5: Results for molecular groups, functional groups, and phase states for size-resolved atmospheric aerosol (stages 7 – 9) from periods of both day and nighttime as measured by scanning transmission X-ray microscopy with near-edge X-ray absorption fine structure spectroscopy (STXM – NEXAFS). Numerical values represent number of particles per classification.

	Dayime (August 2, 2021)			
	Stage 7	Stage 8	Stage 9	Average ± SD
Molecular Group				
OC	246 (98%)	458 (92%)	659 (84%)	(91 ± 7) %
EC	4 (2%)	38 (8%)	126 (16%)	(9 ± 7) %
IN	-	-	-	-
OC+EC+IN	-	-	-	-
Total Particles	250	496	785	
Functional Group				
Alkene	22%	13%	13%	(16 ± 5) %
Carbonyl	16%	15%	15%	(15 ± 1) %
Aliphatic	13%	13%	14%	(13 ± 1) %
Amide	0%	0%	0%	-
Carboxylic	29%	31%	30%	(30 ± 1) %
Alcohol	24%	26%	27%	(26 ± 2) %
Carbonate	1%	2%	1%	(1 ± 1) %
Phase State				
Liquid	6%	46%	30%	(27 ± 20) %
Semi-solid	77%	46%	64%	(62 ± 16) %
Solid	17%	8%	6%	(10 ± 6) %
	Nighttime (August 2, 2021)			
	Stage 7	Stage 8	Stage 9	Average ± SD
Molecular Group				
OC	143 (94%)	366 (97%)	396 (94%)	(95 ± 2) %
EC	9 (6%)	11 (3%)	14 (3%)	(4 ± 2) %
IN	-	-	9 (2%)	(3 ± 5) %
OC+EC+IN	-	-	1 (0.2%)	(0 ± 1) %
Total Particles	152	377	420	
Functional Group				
Alkene	13%	14%	18%	(15 ± 3) %
Carbonyl	16%	15%	19%	(17 ± 2) %
Aliphatic	12%	11%	10%	(11 ± 1) %
Amide	0%	0%	1%	(0 ± 1) %
Carboxylic	33%	36%	27%	(32 ± 5) %
Alcohol	25%	22%	24%	(24 ± 2) %
Carbonate	1%	2%	1%	(1 ± 1) %
Phase State				
Liquid	3%	37%	39%	(26 ± 20) %
Semi-solid	62%	54%	59%	(58 ± 4) %
Solid	35%	9%	2%	(15 ± 17) %

Table S6: Results for molecular groups and phase states for size-resolved atmospheric aerosol (stages 7 – 9) from periods of both day and nighttime as measured by computer-controlled scanning electron microscopy with energy-dispersive X-ray spectroscopy (CCSEM – EDX). Numerical values indicate number of particles per classification.

	Day (August 2, 2021)			
	Stage 7	Stage 8	Stage 9	Average ± SD
Molecular Group				
CNO	1059 (87%)	1910 (96%)	413 (99%)	(94 ± 1) %
CNOS	146 (12%)	69 (3%)	4 (1%)	(5 ± 6) %
Na Rich Particles	3 (0.2%)	0 (0%)	0 (0%)	(0.1 ± 0.1) %
Dust	10 (0.8%)	6 (0.4%)	0 (0%)	(0.4 ± 0.4) %
Total Particles	1218	2826	417	
Phase State				
Liquid	97 (65%)	148 (99%)	140 (89%)	(84 ± 18) %
Semi-Solid	22 (15%)	2 (1%)	11 (7%)	(8 ± 7)%
Solid	31 (21%)	0 (0%)	6 (4%)	(8 ± 11)%
Total Particles	150	150	157	
	Night (August 3, 2021)			
	Stage 7	Stage 8	Stage 9	Average ± SD
Molecular Group				
CNO	3831 (84%)	1218 (91%)	609 (94%)	(90 ± 5) %
CNOS	681 (15%)	126 (9%)	27 (4%)	(9 ± 6) %
Na Rich Particles	11 (0.2%)	0 (0%)	1 (0.2%)	(0.1 ± 0.1) %
Dust	37 (0.8%)	1 (0.1%)	14 (2%)	(1 ± 1) %
Total Particles	4560	1345	651	
Phase State				
Liquid	87 (57%)	139 (90%)	138 (92%)	(80 ± 20) %
Semi-Solid	21 (14%)	11 (7%)	5 (3%)	(8 ± 6)%
Solid	45 (29%)	4 (3%)	7 (5%)	(12 ± 14)%
Total Particles	153	154	150	

Table S7: Results for molecular groups, aromaticity indexes and phase states for size-resolved atmospheric aerosol (stages 7 – 9) from periods of both day and nighttime as measured by nanospray desorption electrospray ionization with 21 Tesla Fourier transform ion cyclotron resonance mass spectrometry (nano-DESI 21T FTICR MS). Numerical values indicate number of assigned molecular formulae. Note that the results presented here are based upon number of assigned molecular formulae, whereas those presented within the main text are weighted according to signal abundance.

	Day (August 2, 2021)			
	Stage 7	Stage 8	Stage 9	Average ± SD
Molecular Group				
CHO	1083 (75%)	1231 (72%)	1063 (74%)	(74 ± 2) %
CHNO	362 (25%)	468 (28%)	366 (26%)	(26 ± 2) %
Total Mol. Formulae	1445	1699	1429	
Aromaticity Index				
Condensed Aromatic	20 (1%)	25 (1%)	16 (1%)	(1 ± 0) %
Aromatic	116 (8%)	143 (8%)	114 (8%)	(8 ± 0) %
High O Unsaturated	806 (56%)	904 (53%)	765 (54%)	(54 ± 2) %
Low O Unsaturated	315 (22%)	374 (22%)	326 (23%)	(22 ± 1) %
Aliphatic	188 (13%)	253 (15%)	208 (15%)	(14 ± 1) %
Total Mol. Formulae	1445	1699	1429	
Oxidation Information				
O/C	0.6 ± 0.2	0.6 ± 0.2	0.6 ± 0.2	0.6 ± 0
OS_C	0.0 ± 0.4	0.0 ± 0.4	0.0 ± 0.4	0.0 ± 0
Phase State				
Liquid	4%	4%	4%	(4 ± 0) %
Semi-solid	37%	38%	41%	(39 ± 2) %
Solid	60%	58%	55%	(58 ± 3) %
	Night (August 3, 2021)			
	Stage 7	Stage 8	Stage 9	Average ± SD
Molecular Group				
CHO	1123 (75%)	1221 (75%)	927 (83%)	(78 ± 5) %
CHNO	367 (25%)	411 (25%)	194 (17%)	(22 ± 5) %
Total Mol. Formulae	1490	1632	1121	
Aromaticity Index				
Condensed Aromatic	21 (1%)	25 (2%)	14 (1%)	(1 ± 1) %
Aromatic	119 (8%)	136 (8%)	84 (7%)	(8 ± 1) %
High O Unsaturated	812 (54%)	849 (52%)	608 (54%)	(53 ± 2) %
Low O Unsaturated	346 (23%)	371 (23%)	259 (23%)	(23 ± 0) %
Aliphatic	192 (13%)	251 (15%)	156 (14%)	(14 ± 1) %
Total Mol. Formulae	1490	1632	1121	
Oxidation Information				
O/C	0.6 ± 0.2	0.6 ± 0.2	0.6 ± 0.2	0.6 ± 0.0
OS_C	0.0 ± 0.5	0.0 ± 0.4	0.0 ± 0.4	0.0 ± 0.0

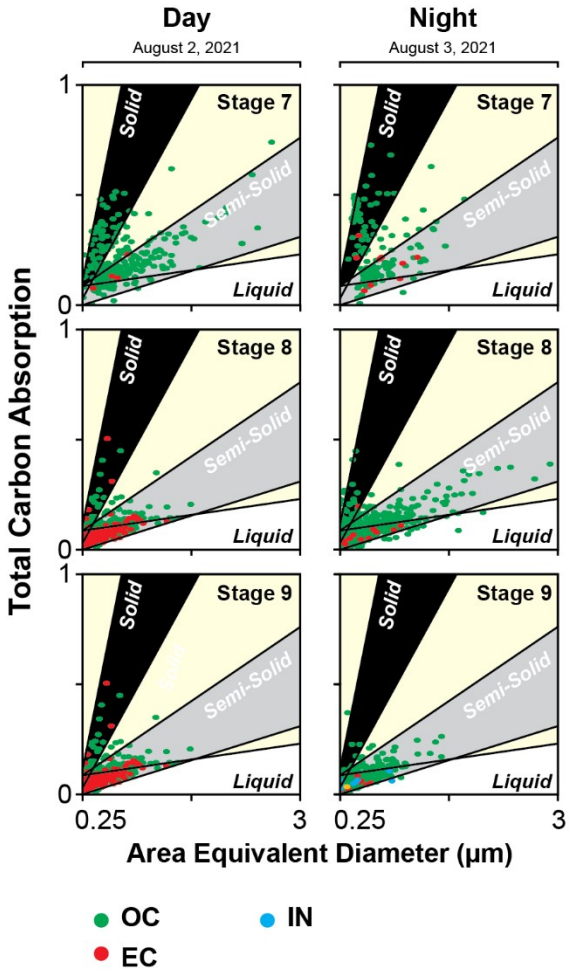

Figure S9: Total carbon absorption (TCA) versus area equivalent diameter as measured by scanning transmission X-ray microscopy with near-edge X-ray absorption fine structure spectroscopy (STXM – NEXAFS) for determination of individual particle phase state. Particles may additionally be individually classified as 'OC', 'IN', 'EC', or 'OC + EC + IN' as described in the main manuscript.

References

(1) AirNow https://www.airnow.gov/ (accessed Jul 3, 2023).

(2) Cheng, Z.; Sharma, N.; Tseng, K.-P.; Kovarik, L.; China, S. Direct Observation and Assessment of Phase States of Ambient and Lab-Generated Sub-Micron Particles upon Humidification. *RSC Adv.* **2021**, *11* (25), 15264–15272. https://doi.org/10.1039/D1RA02530A.

(3) Shiraiwa, M.; Li, Y.; Tsimpidi, A. P.; Karydis, V. A.; Berkemeier, T.; Pandis, S. N.; Lelieveld, J.; Koop, T.; Pöschl, U. Global Distribution of Particle Phase State in Atmospheric Secondary Organic Aerosols. *Nat. Commun.* **2017**, *8*, 1–7. https://doi.org/10.1038/ncomms15002.

(4) Schmedding, R.; Rasool, Q. Z.; Zhang, Y.; Pye, H. O. T.; Zhang, H.; Chen, Y.; Surratt, J. D.; Lopez-Hilfiker, F. D.; Thornton, J. A.; Goldstein, A. H.; Vizuete, W. Predicting Secondary Organic Aerosol Phase State and Viscosity and Its Effect on Multiphase Chemistry in a Regional-Scale Air Quality Model. *Atmos. Chem. Phys.* **2020**, *20* (13), 8201–8225. https://doi.org/10.5194/acp-20-8201-2020.

(5) Lata, N. N.; Zhang, B.; Schum, S.; Mazzoleni, L.; Brimberry, R.; Marcus, M. A.; Cantrell, W. H.; Fialho, P.; Mazzoleni, C.; China, S. Aerosol Composition, Mixing State, and Phase State of Free Tropospheric Particles and Their Role in Ice Cloud Formation. *ACS Earth Sp. Chem.* **2021**, *5* (12), 3499–3510. https://doi.org/10.1021/acsearthspacechem.1c00315.

(6) Tomlin, J. M.; Jankowski, K. A.; Rivera-Adorno, F. A.; Fraund, M.; China, S.; Stirm, B. H.; Kaeser, R.; Eakins, G. S.; Moffet, R. C.; Shepson, P. B.; Laskin, A. Chemical Imaging of Fine Mode Atmospheric Particles Collected from a Research Aircraft over Agricultural Fields. *ACS Earth Sp. Chem.* **2020**, *4* (11), 2171–2184. https://doi.org/10.1021/acsearthspacechem.0c00172.

(7) Reid, J. P.; Bertram, A. K.; Topping, D. O.; Laskin, A.; Martin, S. T.; Petters, M. D.; Pope, F. D.; Rovelli, G. The Viscosity of Atmospherically Relevant Organic Particles. *Nat. Commun.* **2018**, *9* (1), 956. https://doi.org/10.1038/s41467-018-03027-z.

(8) Cui, M. Introduction to the K-Means Clustering Algorithm Based on the Elbow Method. *Accounting, Audit. Financ.* **2020**, *1* (1), 5–8.

(9) Tivanski, A. V; Hopkins, R. J.; Tyliszczak, T.; Gilles, M. K. Oxygenated Interface on Biomass Burn Tar Balls Determined by Single Particle Scanning Transmission X-Ray Microscopy. *J. Phys. Chem. A* **2007**, *111* (25), 5448–5458. https://doi.org/10.1021/jp070155u.

(10) Pham, D. Q.; O'Brien, R.; Fraund, M.; Bonanno, D.; Laskina, O.; Beall, C.; Moore, K. A.; Forestieri, S.; Wang, X.; Lee, C.; Sultana, C.; Grassian, V.; Cappa, C. D.; Prather, K. A.; Moffet, R. C. Biological Impacts on Carbon Speciation and Morphology of Sea Spray Aerosol. *ACS Earth Sp. Chem.* **2017**, *1* (9), 551–561. https://doi.org/10.1021/acsearthspacechem.7b00069.

(11) Moffet, R. C.; Tivanski, A. V; Gilles, M. K. Fundamentals and Applications in Aerosol Spectroscopy; Signorell, R., Reid, J. P., Eds.; 2011; pp 243–272.

(12) Moffet, R. C.; Henn, T.; Laskin, A.; Gilles, M. K. Automated Chemical Analysis of Internally Mixed Aerosol Particles Using X-Ray Spectromicroscopy at the Carbon K-Edge. *Anal. Chem.* **2010**, *82* (19), 7906–7914. https://doi.org/10.1021/ac1012909.

(13) Fraund, M.; Bonanno, D. J.; China, S.; Pham, D. Q.; Veghte, D.; Weis, J.; Kulkarni, G.; Teske, K.; Gilles, M. K.; Laskin, A.; Moffet, R. C. Optical Properties and Composition of Viscous Organic

Particles Found in the Southern Great Plains. *Atmos. Chem. Phys.* **2020**, *20* (19), 11593–11606. https://doi.org/10.5194/acp-20-11593-2020.

(14) Moffet, R. C.; Rödel, T. C.; Kelly, S. T.; Yu, X. Y.; Carroll, G. T.; Fast, J.; Zaveri, R. A.; Laskin, A.; Gilles, M. K. Spectro-Microscopic Measurements of Carbonaceous Aerosol Aging in Central California. *Atmos. Chem. Phys.* **2013**, *13* (20), 10445–10459. https://doi.org/10.5194/acp-13-10445-2013.

(15) Kroll, J. H.; Donahue, N. M.; Jimenez, J. L.; Kessler, S. H.; Canagaratna, M. R.; Wilson, K. R.; Altieri, K. E.; Mazzoleni, L. R.; Wozniak, A. S.; Bluhm, H.; Mysak, E. R.; Smith, J. D.; Kolb, C. E.; Worsnop, D. R. Carbon Oxidation State as a Metric for Describing the Chemistry of Atmospheric Organic Aerosol. *Nat. Chem.* **2011**, *3* (2), 133–139. https://doi.org/10.1038/nchem.948.

(16) Li, Y.; Pöschl, U.; Shiraiwa, M. Molecular Corridors and Parameterizations of Volatility in the Chemical Evolution of Organic Aerosols. *Atmos. Chem. Phys.* **2016**, *16* (5), 3327–3344. https://doi.org/10.5194/acp-16-3327-2016.

(17) Koch, B. P.; Dittmar, T. From Mass to Structure: An Aromaticity Index for High-Resolution Mass Data of Natural Organic Matter. *Rapid Commun. Mass Spectrom.* **2006**, *20* (5), 926–932. https://doi.org/https://doi.org/10.1002/rcm.2386.

(18) Koch, B. P.; Dittmar, T. From Mass to Structure: An Aromaticity Index for High-Resolution Mass Data of Natural Organic Matter. *Rapid Commun. Mass Spectrom.* **2016**, *30* (1), 250. https://doi.org/https://doi.org/10.1002/rcm.7433.

(19) Upshur, M. A.; Strick, B. F.; McNeill, V. F.; Thomson, R. J.; Geiger, F. M. Climate-Relevant Physical Properties of Molecular Constituents for Isoprene-Derived Secondary Organic Aerosol Material. *Atmos. Chem. Phys.* **2014**, *14* (19), 10731–10740. https://doi.org/10.5194/acp-14-10731-2014.

(20) Vaden, T. D.; Imre, D.; Beránek, J.; Shrivastava, M.; Zelenyuk, A. Evaporation Kinetics and Phase of Laboratory and Ambient Secondary Organic Aerosol. *Proc. Natl. Acad. Sci.* **2011**, *108* (6), 2190–2195. https://doi.org/10.1073/pnas.1013391108.